# Observation of liquid crystals confined in an elliptic cylinder

Joonwoo Jeong and Mahn Won Kim

# Observation of liquid crystals confined in an elliptic cylinder

Joonwoo Jeong and Mahn Won Kim[a)]

*Department of Physics, KAIST, Daejeon 305-701, South Korea*

We present the observation of liquid crystals confined in elliptic cylinders. To fabricate the elliptic cylinder, poly(dimethlysiloxane) micro-channels having circular cross sections are stretched uniaxially along the direction of the diameter. Upon increasing the aspect ratio of the elliptic cross section, confined nematic liquid crystals maintain their escaped-radial configuration with homeotropic anchoring. In smectic-A liquid crystals, defect regions of focal conic domains appear as a function of the aspect ratio. We propose a model to understand the formation of these defects in terms of the confinement-induced misorientation, and resultant tilt grain boundaries. © 2012 American Institute of Physics. [http://dx.doi.org/10.1063/1.4745773]

Confined liquid crystals (LCs) can have a variety of structures depending on the balance between bulk elastic energy and surface anchoring energy.[1–3] Cylindrical confinements, a form of symmetric confinement, have been employed to study these various structures and the properties of LCs.[4–8] For example, an escaped-radial configuration[9–12] and beaded-core defects[13–15] are observed in cylinders. In addition, the elastic constants and the anchoring energy of LCs have been determined from observation of confined LCs.[16–19]

Here, we present the observation of LCs confined in elliptic cylinders with homeotropic anchoring. The cross sections of the elliptic cylinders are ellipses that have a continuously varying curvature. While controlling the size and shape of these elliptic cross sections, we demonstrate that nematic LCs maintain the escaped-radial configuration and smectic-A LCs exhibit the defects of focal conic domains (FCDs).

Elastomeric microchannels are used as cylindrical confinements. We utilize capillaries as scaffolds to make poly (dimethlysiloxane) (PDMS) micro-channels having circular cross sections.[20] We pour a mixture of a PDMS pre-polymer and a curing agent (Sylgard 184 kit, Dow Corning, Midland, MI, USA) in a weight ratio of 10:1 on the scaffolds. The scaffolds are made of polyimide-coated fused silica capillaries (Polymicro Technologies, Phoenix, AZ, USA)/polycarbonate capillaries (Paradigm Optics, Inc., WA, USA) and double-sided adhesive tape as spacers (3M, St. Paul, MN, USA).[21] Then, as shown in Fig. 1(a), the capillary is pulled out from the cured PDMS to produce a channel having a circular cross section. This PDMS slab is mounted on a custom-built tensile tester that stretches the slab along the direction of the diameter using a micrometer.

After filling the channel by capillarity with LCs, 4′-octyl-4-biphenylcarbonitrile (8CB), we observe the LC configurations as a function of the strain of the PDMS slab. To obtain the equilibrium configuration in the circular channel, the LCs are heated over the nematic-isotropic transition point and cooled back to the nematic or smectic-A phase. The temperature and the phase of the LCs are then maintained during stretching of the PDMS slab. As shown in Fig. 2, bright-field images of the *xz*-plane are collected according to the LC phase as a function of the strain of the PDMS slab. Polarized optical microscopy (POM) images are also taken with two different directions of crossed polarizers and polychromatic illumination from a halogen lamp.

When the circular channel is stretched along the direction of the diameter, the cross section becomes an ellipse, as shown in Fig. 1(b). These bright-field images of cross sections are well fitted into ellipses. We define the aspect ratio as the ratio of the semi-major axis *a* to the semi-minor axis *b*. To estimate this aspect ratio, we employ a model based on the Poisson's ratio instead of *ex situ* measurements of the cross-sectional axes.[21] We assume that the channel can be considered as a cylindrical hole in an infinite solid under remote loading along the *x*-axis.[22] In this problem, the displacements *u* of the boundary along *x* and *y* are given by Eq. (1),

$$u_x = 6\left(\frac{\sigma_0(1+\nu)R}{2E}\right)(1-\nu)\cos\theta$$

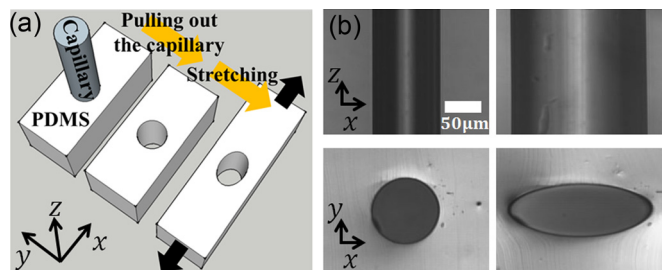$$u_y = -2\left(\frac{\sigma_0(1+\nu)R}{2E}\right)(1-\nu)\sin\theta. \qquad (1)$$



FIG. 1. Fabrication of elliptic cylindrical confinement. (a) A schematic diagram of how to fabricate the elliptic cylindrical hole in a PDMS slab. The arrows in the lower left corner represent the *x*, *y*, and *z* axes of Cartesian coordinates. (b) Bright-field microscopy images of empty cylindrical holes. The top row shows *xz*-plane images of channels. The right column shows channels that are stretched along the direction of the diameter. The bottom row shows *xy*-plane images of the above channels. Note that *xy*-plane images are taken at the end of the channel.

[a)]Author to whom correspondence should be addressed. Electronic mail: mwkim@kaist.ac.kr.
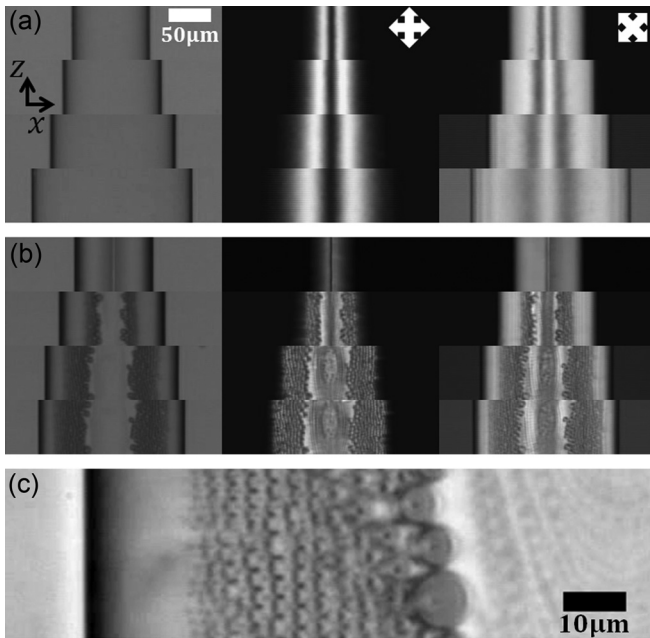
FIG. 2. Optical microscopy images of LCs confined in a cylinder according to LC phase and strain of the PDMS slab. (a) Nematic phase. (b) Smectic-A phase. The first column shows bright-field images. The second and third columns are POM images. The white arrows in the upper right corners represent the directions of the crossed polarizer. (c) A magnified bright-field image of smectic-A LCs confined in an elliptic cylinder. Note that, to observe the defect region clearly, we enhance the contrast of this image.

$R$ is the radius of the cylindrical hole and $\sigma_0$ is the tensile stress. $E$ and $\nu$ are Young's modulus and Poisson's ratio for the solid, respectively. Considering these displacements and the parametric equation of a circle $(R\cos\theta, R\sin\theta)$, we prove that the cross section of a stretched cylindrical hole is an ellipse, of which the parametric equation is $(A\cos\theta, B\sin\theta)$ when $A$ and $B$ are numerical constants. In addition, the effective Poisson's ratio of the cylindrical hole $\nu' = -u_y/u_x$ is 1/3 regardless of $\nu$.

Using the integrated form of the definition of Poisson's ratio $(1 + \Delta R_x/R)^{-\nu'} = (1 - \Delta R_y/R)$, the aspect ratio of the deformed channel is given by Eq. (2),

$$\frac{a}{b} = \frac{R + \Delta R_x}{R - \Delta R_y} = \left(\frac{R + \Delta R_x}{R}\right)^{1+\nu'}. \tag{2}$$

$\Delta R_x$ and $\Delta R_y$ are length changes in the $x$ and $y$ directions, respectively. Using $\nu' = 1/3$, we can estimate the aspect ratio by measuring $R$ and $R + \Delta R_x = a$ only in the $xz$-plane, as shown in Fig. 2.

In Fig. 2(a), nematic LCs have escaped-radial configurations[9–11] in the elliptic cylindrical confinement with homeotropic anchoring. In the POM images with crossed polarizers in a diagonal direction, we identify two broad dark lines that are observed typically in the escaped-radial configuration. Additionally, we frequently observe singular points where the bend direction changes.[21] Note that birefringence of the highly stretched PDMS results in a bright background in the POM images with the diagonal crossed polarizers.[23]

As shown in Figs. 2(b) and 2(c), defect regions of closely packed FCDs appear in smectic-A LCs.[24,25] In Fig. 2(c), the typical texture of FCDs can be recognized. In

addition, the region near the cylindrical axis also appears to have defects that are different from FCDs. The structure of these defects is still under investigation. Note that the width of a defect-free region is defined by the distance from the channel wall to the position where the defects start to appear.[21]

Fig. 3 shows how the width of the defect-free region changes as the aspect ratio of the channel increases. In Fig. 3(a), we concatenate images of a single stretched channel in the order of the aspect ratio. In Fig. 3(b), to compare the widths of the defect-free regions regardless of the channel size, the widths are normalized to the semi-major axis $a$. Error bars are the sample standard deviations of five measured widths, and most of them are smaller than the symbols. Note that the minimum aspect ratio $\zeta$ where the FCDs start to appear depends on the size of the channel as shown in Fig. 3(c).[21] Furthermore, the channel of 28 $\mu$m in diameter,
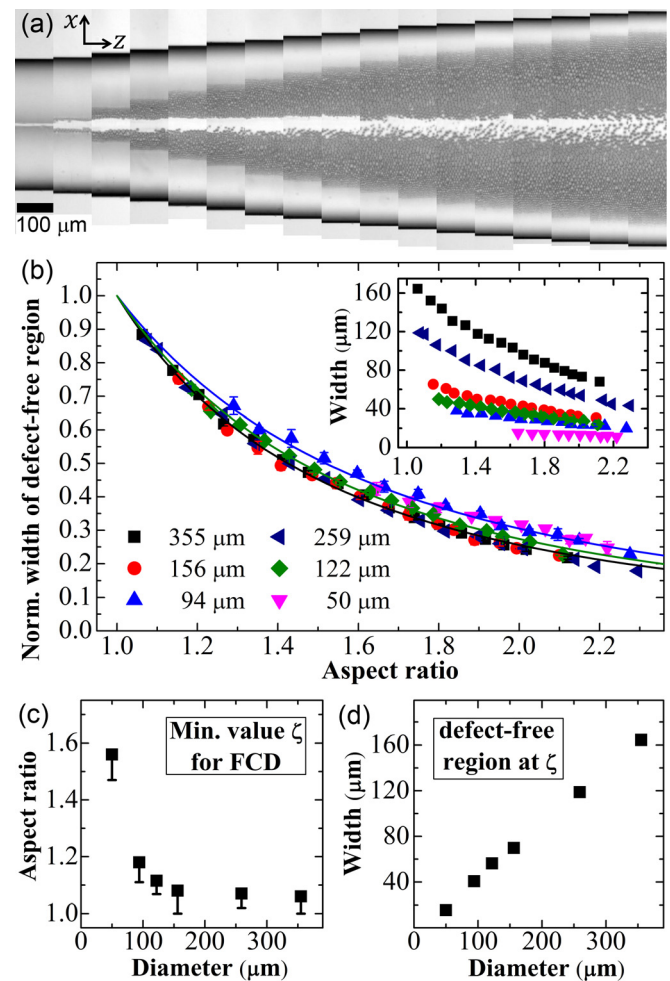


FIG. 3. The defect region as a function of the aspect ratio of a channel. (a) An image sequence of smectic-A LCs confined in an elliptic cylinder in the order of the aspect ratio. Note that each image is taken in the middle of the channel and is contrast-enhanced. (b) The normalized width of the defect-free region as a function of the aspect ratio of the channel. Each symbol represents the data from 6 channels of different sizes. The legend represents the diameters of their undeformed circular cross sections. Solid lines are fitting results obtained using Eq. (4). The inset plots the absolute width of the defect-free region as a function of the aspect ratio. (c) The minimum aspect ratio $\zeta$ where FCDs start to appear. The $x$-axis of (c) is a diameter of a circular channel. The error bars represent the measured maximum aspect ratio without FCDs. (d) The width of the defect-free region at $\zeta$ as a function of a channel size.

the smallest one, does not show FCDs in the experimental range of the aspect ratio.[26] Fig. 3(d) shows the width of the defect-free region at $\zeta$ according to the diameter of the channel.

In smectic-A LCs, we assume that smectic layers of the same thickness are parallel to each other and to the interface due to homeotropic anchoring.[27,28] In Fig. 4, the dotted lines represent the ellipse's equidistant curves, which are parallel to the smectic layers. Directors of LC molecules lie on the normal lines of these curves. The normal lines intersect the major axis of the ellipse at an angle $\theta$ with the $x$-intercept $(x', 0)$. Considering the equation of the ellipse $x^2/a^2 + y^2/b^2 = 1$ and the equation of a line normal to the ellipse at $(X, Y)$, we can get Eq. (3) when $a^2 Y/b^2 X = \tan\theta$,

$$\frac{x'}{a} = \frac{a/b - b/a}{\sqrt{\tan^2\theta + (a/b)^2}}. \tag{3}$$

The major axis of the ellipse can be considered as a tilt grain boundary of which the misorientation angle $\theta$ continuously changes. This non-zero $\theta$ leads to dilation of the smectic layers. The inset in Fig. 4 shows that smectic layers around the major axis are bent through $2\theta$ and thus become dilated, $d > d_0$, where $d$ is the thickness of a single smectic layer on the major axis and $d_0$ is the undeformed thickness. Equation (3) implies that the misorientation angle and the dilation increase when $(x', 0)$ moves from $(a,0)$ to $(0,0)$. Note that $\theta$ is 0° from $(a, 0)$ to $((a^2 - b^2)/a, 0)$, which is the center of curvature at $(a, 0)$ of the ellipse.

From the perspective of the tilt grain boundary, the region of small $\theta$ corresponds to a curvature wall.[29] The elastic free energy per unit area of the curvature wall[30] is a monotonically increasing function of $\theta$, which is proportional to $\cos\theta(\tan\theta - \theta)$. Then, if $\theta$ exceeds a critical misorientation angle $\gamma$, smectic layers can lower the elastic free energy by creating defects such as FCDs or dislocations. These defects compose FCD walls or dislocation walls at the tilt grain boundary.[25,29]
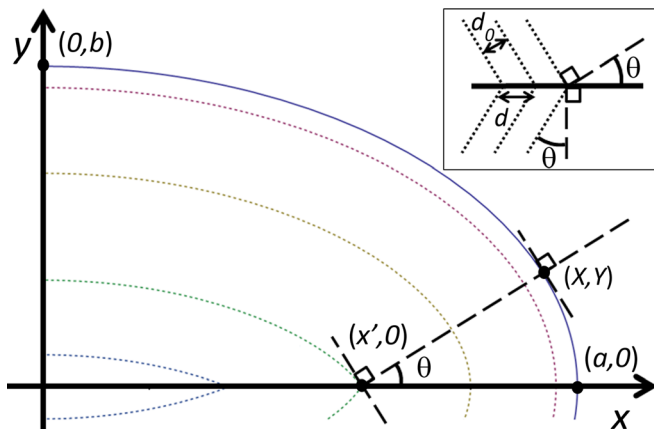


FIG. 4. A schematic diagram of smectic layers in the elliptic cross section. The ellipse of a solid line represents the boundary of the confinement. The dotted lines are equidistant curves of the ellipse, and are parallel to the smectic layers. The dotted lines in the inset, which magnifies the region around $(x', 0)$, represent the smectic layers of thickness $d_0$. $d$ is the thickness in the dilated region.

Under the assumption that the critical misorientation angle $\gamma$ is mainly determined in the misoriented region localized around the major axis, we hypothesize that $\gamma$ is independent of the shape of the channel, the aspect ratio. Using Eq. (3), we estimate the critical misorientation angle $\gamma$, where the FCDs start to appear. Equation (4) gives the relation between the normalized width of the defect-free region $(W/a)$ and the aspect ratio $(a/b)$ with a single parameter $\gamma$, when $W$ is the width of the defect-free region and $x'/a = 1 - W/a$, $\theta = \gamma$ in Eq. (3),

$$\frac{W}{a} = 1 - \frac{a/b - b/a}{\sqrt{\tan^2\gamma + (a/b)^2}}. \tag{4}$$

The solid lines in Fig. 3(b) are the fitting results to provide the value of $\gamma$ using this relation. Note that data from the channels of 355 $\mu$m, 259 $\mu$m, and 156 $\mu$m diameter almost overlap,[21] and they are fitted best by the curves of $\gamma = 11\pm3°$. The data from the 122 $\mu$m channel are fitted by the curve of $\gamma = 26\pm2°$. The data from the 94 $\mu$m and 50 $\mu$m channel also overlap, and they are described well by the curve of $\gamma = 39\pm2°$.

To gain insight into this critical misorientation angle in terms of elastic free energy, we employ a model that compares the elastic free energy per unit area of the curvature wall and the FCD wall. Equation (5) gives the ratio between the energy of the curvature wall $E_{curv}$ and the energy of the FCD wall $E_{FCD}^{curv}$ in which the residual areas are relaxed by the curvature walls,[25]

$$\frac{E_{curv}}{E_{FCD}^{curv}} \sim \left(\frac{L}{\lambda}\right)^{2-n} \theta^{7-3n}. \tag{5}$$

$L$ is the size of the largest circles of toric FCDs, when we project the observed FCDs into the plane which is perpendicular to the asymptotic direction. From the region where the defects start to appear in Fig. 2(c), we estimate $L$ is of the order of 1 $\mu$m, which is the optically observed minimum size of FCDs in our experiment.[21] $\lambda$ is the penetration length, which is of the order of 1 nm. In addition, the exponent $n$ is approximately 1.3 by numerical calculations.[31] Then, $\theta = \gamma$ where $E_{curv}$ is comparable to $E_{FCD}^{curv}$ is roughly 10°. It is worthwhile to note that this theoretical estimation is quite similar to the fitted $\gamma$ of larger channels such as the 355 $\mu$m diameter channel.

The observed size-dependency may result from the fact that the defects of micron sizes are forbidden in a small $\theta$ region of small channels. In Eq. (3), $\Delta x'$ over a constant $\Delta\theta$ depends on the size of the channel. For example, when the aspect ratio of the 94 $\mu$m channel is the minimum aspect ratio for FCD $\zeta = 1.18$, $x'(\theta = 10°) - x'(\theta = 20°)$ is only about 0.5 $\mu$m from Eq. (3). This $\Delta x'$ is too small to make FCDs of micron size. In other words, the defects of $L \sim 1$ $\mu$m are forbidden in this small $\theta$ region of the 94 $\mu$m channel, and they appear at a larger $\theta$. On the other hand, because $\Delta x'$ is proportional to $R$, the 355 $\mu$m channel can have the defects at this small $\theta$. For this reason, as shown in Fig. 3(c), the minimum aspect ratio $\zeta$ where the FCDs start to appear depends on the size of the channel.[21] To fully understand this size-dependency, we

need an elastic free energy model that considers continuously varying misorientation angle and the size of FCDs.

In summary, by introducing a method to fabricate channels of elliptic cross sections, we have observed nematic/smectic-A LCs confined in elliptic cylinders. The configurations of the nematic and smectic-A LCs can be described as an escaped-radial configuration and tilt grain boundaries, respectively. Our understanding of properties and defects of LCs may benefit from further analysis of these configurations. In addition, these LC configurations controlled by the shape of confining boundaries may be utilized in LC applications such as lithographies using LCs[32,33] and LC lenses.[34,35] The elliptic confinement is applicable also to other organic and soft materials for the study of the effect of confinement on their structures.

[1]P. G. de Gennes and J. Prost, *The Physics of Liquid Crystals*, International Series of Monographs on Physics (Oxford University Press, USA, 1995).

[2]*Liquid Crystals In Complex Geometries: Formed by Polymer And Porous Networks*, edited by G. P. Crawford and S. Zumer (Taylor & Francis, 1996).

[3]M. Kleman and O. D. Lavrentovich, *Soft Matter Physics: An Introduction* (Springer, 2002).

[4]I. Vilfan, M. Vilfan, and S. Žumer, Phys. Rev. A **43**, 6875 (1991).

[5]G. Crawford, R. Ondris-Crawford, S. Žumer, and J. Doane, Phys. Rev. Lett. **70**, 1838 (1993).

[6]M. Ambrozcaroniccaron and S. Zcaronumer, Phys. Rev. E **54**, 5187 (1996).

[7]M. Ambrožič and S. Žumer, Phys. Rev. E **59**, 4153 (1999).

[8]P. Kossyrev, M. Ravnik, and S. Žumer, Phys. Rev. Lett. **96**, 048301 (2006).

[9]P. Cladis and M. Kléman, J. Phys. (France) **33**, 591 (1972).

[10]C. Williams, P. Pieraski, and P. Cladis, Phys. Rev. Lett. **29**, 90 (1972).

[11]R. B. Meyer, Philos. Mag. **27**, 405 (1973).

[12]C. E. Williams, P. E. Cladis, and M. Kleman, Mol. Cryst. Liq. Cryst. **21**, 355 (1973).

[13]P. E. Cladis, Philos. Mag. **29**, 641 (1974).

[14]P. E. Cladis, J. Phys. Colloq. **37**, C3–137 (1976).

[15]P. E. Cladis and A. E. White, J. Appl. Phys. **47**, 1256 (1976).

[16]G. Crawford, D. Allender, and J. Doane, Phys. Rev. A **45**, 8693 (1992).

[17]G. P. Crawford, J. A. Mitcheltree, E. P. Boyko, W. Fritz, S. Zumer, and J. W. Doane, Appl. Phys. Lett. **60**, 3226 (1992).

[18]A. Scharkowski, G. P. Crawford, S. Žumer, and J. W. Doane, J. Appl. Phys. **73**, 7280 (1993).

[19]R. Polak, G. Crawford, B. Kostival, J. Doane, and S. Žumer, Phys. Rev. E **49**, R978 (1994).

[20]A. Asthana, K.-O. Kim, J. Perumal, D.-M. Kim, and D.-P. Kim, Lab Chip **9**, 1138 (2009).

[21]See supplementary material at http://dx.doi.org/10.1063/1.4745773 for (1) experimental details on the fabrication/observation, (2) the measurements of axes of elliptic cross-sections, (3) additional optical microscopy images of nematic LC with a singular point, (4) how to measure the width of the defect-free region, (5) comparison of theoretical fitting curves, Eq. (4), and (6) bright-field images of FCDs in channels having small aspect ratios.

[22]A. F. Bower, *Applied Mechanics of Solids*, 1st ed. (CRC, Boca Raton, 2009).

[23]B. Erman and P. J. Flory, Macromolecules **16**, 1607 (1983).

[24]C. Williams and M. Kléman, J. Phys. Colloq. **36**, C1–315 (1975).

[25]M. Kléman and O. Lavrentovich, Eur. Phys. J. E **2**, 47 (2000).

[26]In the 28 $\mu$m channel, the FCDs are not observed even when the aspect ratio is increased up to 2.5. Thus, the data of 28 $\mu$m cannot be shown in Figs. 3(b)–3(d). This observation is consistent with the following: $\zeta$ increases steeply when the diameter of the channel decreases in Fig. 3(c) and there seems to be a certain minimum diameter for the formation of FCDs in Fig. 3(d).

[27]C. Blanc and M. Kleman, Eur. Phys. J. E **4**, 241 (2001).

[28]J. Jeong and M. W. Kim, Phys. Rev. Lett. **108**, 207802 (2012).

[29]M. Kleman, *Points, Lines and Walls: In Liquid Crystals, Magnetic Systems and Various Ordered Media* (John Wiley & Sons Inc, 1982).

[30]C. Blanc and M. Kléman, Eur. Phys. J. B **10**, 53 (1999).

[31]P. B. Thomas and D. Dhar, J. Phys. A **27**, 2257 (1994).

[32]J. H. Kim, Y. H. Kim, H. S. Jeong, E. K. Youn, and H.-T. Jung, J. Mater. Chem. **21**, 18381 (2011).

[33]Y. H. Kim, D. K. Yoon, H. S. Jeong, O. D. Lavrentovich, and H.-T. Jung, Adv. Funct. Mater. **21**, 610 (2011).

[34]C. W. Fowler and E. S. Pateras, Ophthalmic Physiol. Opt. **10**, 186 (1990).

[35]I. Abdulhalim, Liq. Cryst. Today **20**, 44 (2011).